

Revisiting the Iconic Spitzer Phase Curve of 55 Cancri e: Hotter Dayside, Cooler Nightside and Smaller Phase Offset

SAMSON J. MERCIER ¹, LISA DANG ¹, ALEXANDER GASS,¹ NICOLAS B. COWAN ^{1,2} AND TAYLOR J. BELL ^{1,3}

¹*Department of Physics, McGill University, 3600 rue University, Montréal, QC H3A 2T8, Canada*

²*Department of Earth & Planetary Sciences, McGill University, 3450 rue University, Montréal, QC H3A 0E8, Canada*

³*BAER Institute, NASA Ames Research Center, Moffett Field, CA 94035, USA*

ABSTRACT

Thermal phase curves of short period exoplanets provide the best constraints on the atmospheric dynamics and heat transport in their atmospheres. The published Spitzer Space Telescope phase curve of 55 Cancri e, an ultra-short period super-Earth, exhibits a large phase offset suggesting significant eastward heat recirculation, unexpected on such a hot planet (Demory et al. 2016b). We present our re-reduction and analysis of these iconic observations using the open source and modular Spitzer Phase Curve Analysis (SPCA) pipeline. In particular, we attempt to reproduce the published analysis using the same instrument detrending scheme as the original authors. We retrieve the dayside temperature ($T_{\text{day}} = 3771_{-520}^{+669}$ K), nightside temperature ($T_{\text{night}} < 1649$ K at 2σ), and longitudinal offset of the planet's hot spot and quantify how they depend on the reduction and detrending. Our re-analysis suggests that 55 Cancri e has a negligible hot spot offset of -12_{-18}^{+21} degrees east. The small phase offset and cool nightside are consistent with the poor heat transport expected on ultra-short period planets. The high dayside $4.5 \mu\text{m}$ brightness temperature is qualitatively consistent with SiO emission from an inverted rock vapour atmosphere.

Keywords: Infrared telescopes — Exoplanet atmospheric composition — Super Earths — Observational astronomy

1. INTRODUCTION

Rocky ultra-short period planets (USPs) are the most amenable terrestrial exoplanets for atmospheric study (for a review, see Winn et al. 2018). Full-orbit Spitzer phasecurves of USPs LHS 3844b (Kreidberg et al. 2019) and K2-141b (Zieba et al. 2022) exhibit no significant hot spot offset and therefore suggest poor day-to-night heat transport. In contrast, $4.5 \mu\text{m}$ Spitzer observations of the best-characterized USP planet, 55 Cancri e (Fischer et al. 2008; Dawson & Fabrycky 2010; Winn et al. 2011; Demory et al. 2011), revealed an eastward phase offset of $\theta_{\text{phase}} = 41 \pm 12$ degrees (Demory et al. 2016b, abbreviated as D16b hereafter).

The Spitzer data, as reduced by D16b, were also re-analyzed by Angelo & Hu (2017) using the phase curve parameterization of Hu et al. (2015). They found an average dayside temperature and a phase curve offset in agreement with D16b, but they obtained a smaller phase curve amplitude suggesting a hotter nightside temperature: 1610_{-130}^{+120} K (Angelo & Hu 2017) cf. 1380_{-450}^{+340} K (D16b). If the Spitzer phase modulation is due to the planet, it suggests effective atmospheric heat circu-

lation. This would be surprising: hot rocky planets are expected to have thin atmospheres (Castan & Menou 2011) and short dayside radiative timescales (Cowan & Agol 2011).

While the phase variations of 55 Cnc e raise many questions, Spitzer IRAC observations are known to be plagued with detector systematics due to the interplay of telescope pointing fluctuations with intra-pixel gain variations. Extracting exoplanets signals at the level of 100 parts per million (ppm) can be therefore extremely challenging and requires the removal of significant instrumental effects (for a review, see Ingalls et al. 2016). Over the past decade, improvements in observing strategy and development of a suite of techniques to remove IRAC time-correlated noise have yielded robust thermal phase curves for many short-period exoplanets (May et al. 2022). However, in addition to the challenges of observing small planets, the 55 Cnc e Spitzer data are particularly complicated to analyze:

1. Since 55 Cnc is a very bright star, the exposure time was reduced to 0.02 s to avoid saturation. Shorter exposures meant more images and hence

frequent interruptions of the observations to downlink data to Earth due to Spitzer’s limited capacity. This, in turn, resulted in the telescope performing multiple visits of 55 Cnc e over the course of a month, as shown in Figure 1. Each visit corresponds to an Astronomical Observation Request (AOR).

2. Because the data were collected over multiple AORs, the target’s position on the IRAC detector varied between observations. The increased spread in centroids means that one has to model the sensitivity of multiple non-overlapping areas of the detector, shown in Figure 1. Since different parts of the detector behave differently, this increased centroid position spread adds significant uncertainty to our planetary inferences.

In this paper, we present a re-reduction and re-analysis of the Spitzer/IRAC phase curve of 55 Cnc e published in D16b but using the Spitzer Phase Curve Analysis pipeline (SPCA¹: Dang et al. 2018; Bell et al. 2021). We first outline our data retrieval, reduction and analysis methods in Section 2. In Section 3 we present our results and discuss the implication of our retrieved phase curve.

2. METHODS

2.1. Data Retrieval

We used observations of the 55 Cnc system (PID 90208, Demory et al. 2012) originally presented by D16b and collected with the 4.5 μm channel of the InfraRed Array Camera (Fazio et al. 2004) aboard the Spitzer Space Telescope (Werner et al. 2004). The observations were taken from 15 June to 15 July 2013 and consist of 8 AORs of continuous time-series observations, each approximately 9 hours in duration, corresponding to half the duration of 55 Cnc e’s orbital period, and with a gap of 3 to 8 days between AORs. The basic Spitzer data calibrated with the S18.18.0 pipeline version were retrieved from the Spitzer Heritage Archive² (DOI: IRSA 2022). The observations were taken in subarray mode with an exposure time of 0.02 s for a total of 4,918,760 frames. We note that AORs 48072704 and 48072960 experienced 30-min long interruptions during observations and therefore exhibit an important jump in the centroids (see Figure 1).

2.2. Data Reduction

Using SPCA, the Spitzer .fits files are first unzipped and loaded into RAM. An initial 4σ clipping is done

along the time axis for each AOR to mask artifacts such as cosmic ray hits or hot pixels. If a masked pixel is within a 5×5 pixel square centered on the target, the frame is ignored entirely. We also evaluate the flux-weighted-mean centroid of the target and the point response function (PRF) width along the x - and y -axis for each frame. Next, frames with flux, centroids or PRF widths differing from the datacube median value along the time axis by 4σ are flagged. We perform photometric extraction with and without these flagged frames, and ultimately choose the photometric scheme resulting in the lowest scatter as explained in the following subsection. Finally, the background flux is subtracted frame by frame and a last 5σ sigma clipping is performed to remove any remaining artifacts. A more in-depth description of the reduction process is provided in Dang et al. (2018) and Bell et al. (2021). The data from all eight AORs totals approximately 70 GB. In order to diminish the computational cost of the model fitting and detrending phase, we chose to bin the data by a factor of 640, or 12.8 s bins (further detailed in Appendix A).

2.3. Photometry

We experimented with Point-Spread Function (PSF) fitting photometry and a variety of circular apertures (soft-edge and hard-edge) with radii ranging from 2.0 to 6.0 pixels. We evaluate the RMS scatter in flux for each photometric scheme of each AOR. We also experiment with a fixed aperture centered on the (14, 15) pixel and a moving aperture centered on the respective centroid of each frame. Ultimately, we find that a moving, soft-edge aperture of radius 2.2 pixels gave us the lowest scatter averaged over all AORs. We therefore adopt this photometric scheme, shown in the right plot of Figure 1, for the remainder of our analysis.

We fit the reduced data with a two-component model accounting for both detector and astrophysical variations. The detector component is essential to remove the intra-pixel sensitivity variations in Spitzer/IRAC data. As shown in the left plot of Figure 1, the centroids are dispersed and 2 AORs are separated into multiple regions (48072704 and 48072960). The large spread of centroids underlines the importance of detrending the detector systematics from the photometric data to distinguish an astrophysical signal. In the right panel of Figure 1, we highlight the two groups of AORs with no overlap in phase: those spanning orbital phases of -0.1 to 0.4, or 0.4 to 0.9. The phase offset obtained by D16b, shown by the black dashed vertical line, occurs at the suture phase for the two groups of AORs, which is suspicious and reinforces the need for a re-reduction and re-analysis.

¹ <https://spca.readthedocs.io/en/v0.3/>

² <https://sha.ipac.caltech.edu/applications/Spitzer/SHA/>

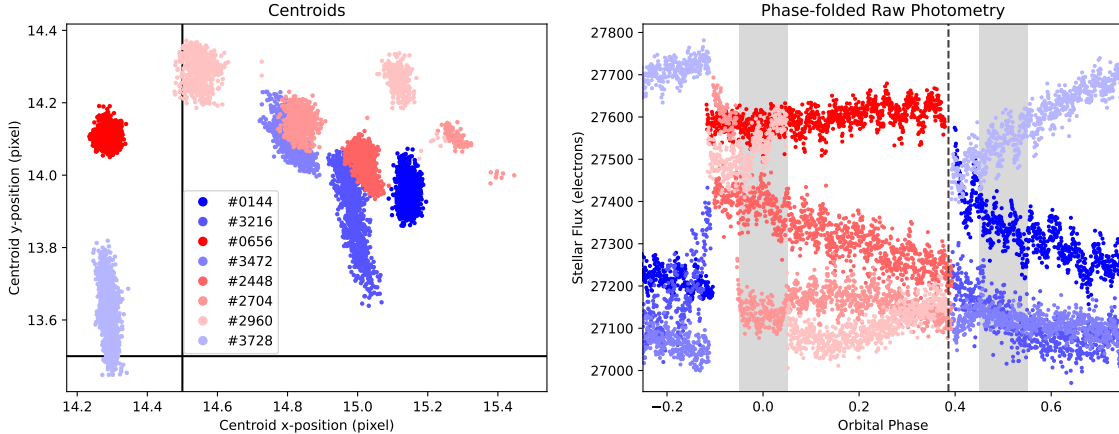


Figure 1. Centroid Position and Raw Photometric data — Plotted on the left is the centroid position on the IRAC detector and on the right is the phase-folded raw photometry obtained from SPCA. In both plots, the 8 AORs are separated into two groups: the red group represents the phase range -0.1 to 0.4 and the blue group represents the phase range 0.4 to 0.9 . The solid black lines on the left plot show the pixel edges. The grey bands in the right plot correspond to the transit (0 phase) and eclipse (0.5 phase) of 55 Cancri e. The black dashed vertical line represents the phase offset obtained by D16b. Note that the offset lines up with the suture point of the two AOR groups around 0.4 orbital phase.

2.4. Astrophysical Model

Our astrophysical model has four components: a constant stellar flux from the host star, a transit, a secondary eclipse, and a first-order sinusoidal phase variation (see section 4.1 in Bell et al. 2021 for further details). We choose to fix astrophysical parameters that are poorly constrained by the Spitzer data to the most up to date values in the NASA Exoplanet Archive³, which can be found in Table 1: inclination i , orbital period P , transit midpoint T_0 , semi-major axis a , eccentricity e , and argument of periastron ω (NASA Exoplanet Archive 2019). These values correspond to the ones reported by Bourrier et al. (2018). We fix the limb-darkening parameters q_1 and q_2 to Claret & Bloemen (2011) estimates, as used in D16b. We let the following astrophysical parameters of interest freely vary: planet-to-star radius ratio R_P/R_* , eclipse depth F_P/F_* and white noise amplitude σ_F , on which we placed uniform priors from 0 to 1, and the two phase variation parameters A and B , on which we placed Gaussian priors (further detail concerning these parameters can be found in Bell et al. 2021). For A the Gaussian prior was $\mu = 0.5, \sigma = 0.5$, and for B the Gaussian prior was $\mu = 0.01, \sigma = 0.5$. We experiment with and without constraints on the brightness map of the planet (Keating & Cowan 2017). More specifically, if we think that the phase curve is not solely planetary in nature, then we do not need to impose a strictly positive phase curve.

These unconstrained phase variations, shown in Figure 2, could be caused by star-planet interactions.

2.5. Detector Model

SPCA offers various detector models, but the one we are most interested in is Bi-Linearly Interpolated Subpixel Sensitivity (BLISS) mapping (Stevenson et al. 2012). Firstly, BLISS is a non-parametric detector model, which reduces the computational cost of model fitting. Secondly, BLISS is particularly well-suited for data sets with large spread in the target’s centroid, which is our case. Lastly, using other detector models such as polynomial detrending would require us to associate one polynomial to each AOR due to the centroids being so spread out. As a result, the number of parameters in our analysis would drastically increase and so would the computational cost. In comparison, BLISS mapping only has 2 hyper-parameters making it the easiest approach to remove detector systematics from this particular data set. D16b also used BLISS mapping on these data.

The BLISS method maps the detector by associating each centroid to a knot. Choosing the right number of knots is key to our analysis. Too few knots would make our model overly simple and unreliable, while too many knots would lead to over-fitting. We decided to use the same number of BLISS knots as D16b, since having similar detector model parameters ensures that our results are comparable. D16b do not report their number of knots, but they specify that at least 5 centroid position points were linked to each knot. After experimenting with various BLISS knot combinations

³ <https://exoplanetarchive.ipac.caltech.edu>

($n_x \times n_y$: 21×16 , 42×32 , 84×64), we determined that $n_x = 84$, $n_y = 64$ gave us approximately 5 centroid position points per knot. As noted by D16b, we also find that combining our BLISS mapping approach with a linear function of the width of the PRF along the x and y axes further reduces the level of correlated noise in the photometric residuals.

Finally, we fit our data and estimate the best fit parameters and uncertainties using `emcee`, a Markov Chain Monte Carlo (MCMC; Foreman-Mackey et al. 2013). We used 150 MCMC walkers and ran a total of 750,000 burn-in steps until convergence upon visual inspection. We then ran a total of 150,000 production steps to sample the posterior distributions for our final parameter and uncertainty estimates.

3. RESULTS & DISCUSSION

3.1. Results

We present the best-fit decorrelated photometry and astrophysical model for the phase variations of 55 Cnc e from our positive-phase-curve fit, shown in the solid black line in Figure 2. We also show D16b’s best-fit astrophysical model for comparison. The peak of the phase variation of both resulting model fit are indicated by vertical dashed lines. We list the astrophysical parameter estimates from the MCMC in Table 1. Our fit shows a transit depth of 291 ± 56 ppm, a secondary eclipse depth of 209^{+50}_{-47} ppm, a phase semi-amplitude of 111^{+17}_{-16} ppm, and a phase offset of 12^{+21}_{-18} degrees west. From our resulting model fit, we derived an average day-side temperature of $3,771^{+670}_{-520}$ K and a nightside temperature of $T_{\text{night}} < 1649$ K at 2σ . Since our unconstrained analysis favors a phase variation with negative flux near transit, the lower uncertainty on the nightside temperature from our constrained analysis is likely underestimated. Therefore, we report a conservative upper limit on the average nightside temperature rather than an estimate.

Our best-fit values for the free parameters differ, sometimes significantly, from those reported by D16b, even though we conservatively inflate our uncertainties according to an Allan plot (see comparison in Table 1). Notably, we conclude that there is no significant offset present in the phase variations. Furthermore, our phase offset does not coincide with the AOR separation at 0.4 orbital phase that can be seen in Figure 1. The potential causes of these discrepancies are detailed in Appendix A. A different photometry extraction strategy is the most likely culprit: we adopt a uniform photometric aperture for all AORs, unlike D16b. The observed scatter could

also be astrophysical in nature, as both Demory et al. (2016a) and Tamburo et al. (2018) have reported eclipse depth variability. Indeed, the astrophysical variability could have been removed by D16b because they used a different photometric aperture for each AOR.

3.2. Interpretation of Results

We adopt the constrained analysis as our fiducial analysis, hypothesizing—as did D16b—that the observed phase variations are solely planetary in nature. Optical monitoring of 55 Cnc e with CHEOPS (Morris et al. 2021) and MOST (Winn et al. 2011; Sulis et al. 2019) revealed phase modulations with ‘negative’ flux values; the system flux drops below the in-eclipse level, which means that the stellar flux is variable. We obtain negative phase variations with our unconstrained analysis, but the semi-amplitude of 172 ppm is greater than that reported in the optical either before (84 ppm; Winn et al. 2011) or after (36 ppm; Morris et al. 2021) the D16b *Spitzer* observations (Table 2). Since it is hard to imagine how stellar variability could impact the IR so much more than the optical, it is unlikely that our unconstrained analysis is affected by the same star-planet interactions as the MOST and CHEOPS observations. For completeness, we report our unconstrained analysis and the best-fit results in Appendix B.

Unlike D16b, our excellent transit depth agreement with Morris et al. (2021) and Meier Valdés et al. (2022) tentatively excludes a cloud-free hydrogen-dominated atmosphere (see details in Appendix D). This is consistent with unsuccessful searches for atoms and molecules in transit (Ehrenreich et al. 2012; Ridden-Harper et al. 2016; Esteves et al. 2017; Tabernero et al. 2020; Zhang et al. 2021b; Keles et al. 2022). While Tsiaras et al. (2016) reported a hint of HCN based on Hubble observations, no molecules—including HCN—were detected in ground-based high-dispersion spectroscopy (Deibert et al. 2021). In the balance, existing transit spectroscopy and broadband photometry suggest that 55 Cnc e has either a high mean molecular mass atmosphere, or no atmosphere at all.

We hypothesize that 55 Cnc e either has a global atmosphere covering both hemispheres of the planet (Hammond & Pierrehumbert 2017) or a local dayside atmosphere (Léger et al. 2011; Castan & Menou 2011; Kite et al. 2016; Zilinskas et al. 2022). In either case, the short radiative timescale on 55 Cnc e ensures there is minimal heat transport, which explains the negligible phase offset and nightside flux. The surprisingly high dayside brightness temperature can be explained with the presence of SiO in the atmosphere. Due to 55 Cnc e’s close proximity to its host star, silicate species present in

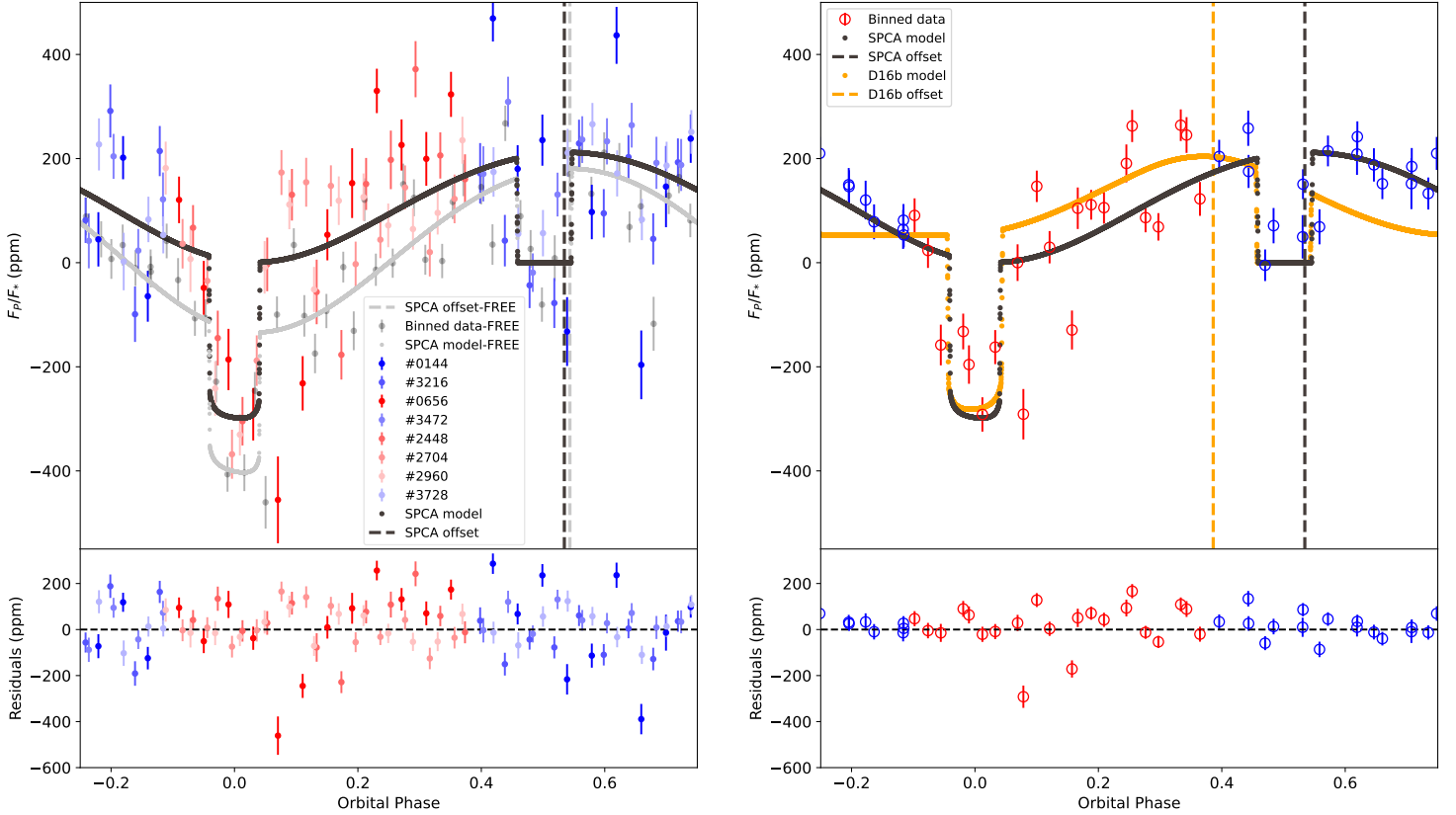


Figure 2. Spitzer/IRAC $4.5 \mu\text{m}$ phase curve of 55 Cancri e — *Top left:* Phase-folded, instrument-detrended Spitzer data and our best fit models. The solid grey line corresponds to our unconstrained analysis where we do not assume that the phase curve is planetary in nature and therefore do not impose a strictly positive phase curve. In our legend, we use the abbreviation FREE for this unconstrained analysis. The red and blue points correspond to decorrelated photometric data for all AORs and, like in Figure 1, we separate them into two groups and distinguish them with different colours. The grey points are the decorrelated photometric data for our unconstrained analysis. For the constrained and unconstrained analyses, the decorrelated photometric data were binned within each AOR by an extra factor of 75 and 150, respectively. *Bottom left:* The residuals for our fiducial, constrained model. *Top right:* The solid black line is our best-fit model using BLISS mapping, same as in the top left plot, and the solid gold line is the best-fit model from D16b. The points represent the decorrelated photometric data for all 8 AORs and, like in Figure 1, we separate them into two groups and distinguish them with different colours. These decorrelated photometric data were binned across all AORs by an extra factor of 165. *Bottom right:* Corresponding residuals for our best-fit model. The error-bars in each plot are the error on the mean within each bin. We have also added vertical lines for the phase offset obtained with our constrained and unconstrained analyses, and by D16b. Neither our constrained or unconstrained fit match that of D16b, despite using the same raw data detrended with BLISS mapping. The constrained fit is our preferred model; it exhibits a large dayside flux, a negligible offset, and small nightside flux.

Table 1. Fixed, Free and Derived Parameters for 55 Cancri e

Parameters	SPCA Values	D16b Values
Fixed Astrophysical Parameters		
i (degrees)	$83.59^{+0.5}_{-0.4}$	$83.3^{+0.9}_{-0.8}$
P (days)	$0.7365474^{+0.0000013}_{-0.0000014}$	0.736539 ± 0.000007
T_0 (days)	$2457063.2096^{+0.0006}_{-0.0004}$	2455733.013 ± 0.007
a/R_*	3.52 ± 0.01	3.514 ± 0.62
e	0.05 ± 0.03	$0.061^{+0.065}_{-0.043}$
ω (degrees)	86^{+31}_{-33}	202^{+88}_{-70}
q_1	0.0286	0.0286
q_2	0.0554	0.0554
Stellar Effective Temperature (K)	5172 ± 18	5250^{+123}_{-172}
Stellar Surface Gravity ($\log_{10}(cm/s^2)$)	4.43 ± 0.02	$4.43^{+0.052}_{-0.14}$
Stellar Metallicity (dex)	0.35 ± 0.10 [Fe/H]	0.35 ± 0.10 [M/H]
checkPhase	True	True
Free Astrophysical Parameters		
R_P/R_*	$0.01708^{+0.0016}_{-0.0017}$	0.0187 ± 0.0007
F_P/F_*	$0.000209^{+0.000050}_{-0.000047}$	0.000154 ± 0.000023
Photometric precision (ppm)	$445.4^{+7.5}_{-7.3}$	363
A	$0.493^{+0.04}_{-0.07}$	Unknown
B	0.108 ± 0.18	Unknown
Detector Hyper Parameters		
x knot resolution	84	Unknown
y knot resolution	64	Unknown
Derived Parameters		
Phase Semi-Amplitude (ppm)	110.9^{+17}_{-16}	75.8 ± 17
Phase Offset (degrees east)	-12.43^{+21}_{-18}	41 ± 12
Average Dayside Temperature (K)	3771^{+669}_{-520}	2999^{+188}_{-193}
Average Nightside Temperature (K)	1045^{+302}_{-243}	1380 ± 400
Conservative Nightside Temperature (K)	(< 1649 2σ , < 1951 3σ)	–

NOTE—D16b report phase semi-amplitude and dayside brightness temperature inconsistent with their plotted best-fit model. We re-calculated their semi-amplitude by removing the transit and eclipse from their Source data (see Footnote 4), and measuring the maximum and minimum values. Their dayside brightness temperature was re-calculated using the formula found in Schwartz et al. (2017). Rather than approximating the spectrum of 55 Cnc as a black body, we used the stellar effective temperature, surface gravity and metallicity reported above to estimate its spectrum using a Phoenix model^a. The error bars on the fixed parameters were not used in our analysis. We inflated the error bars on the retrieved parameters for our fiducial analysis according to a binned residuals—Allan—plot (see Figure 4). The method used to inflate our uncertainties is detailed in Appendix C.

^a <https://www.stsci.edu/hst/instrumentation/reference-data-for-calibration-and-tools/astronomical-catalogs/phoenix-models-available-in-synphot>

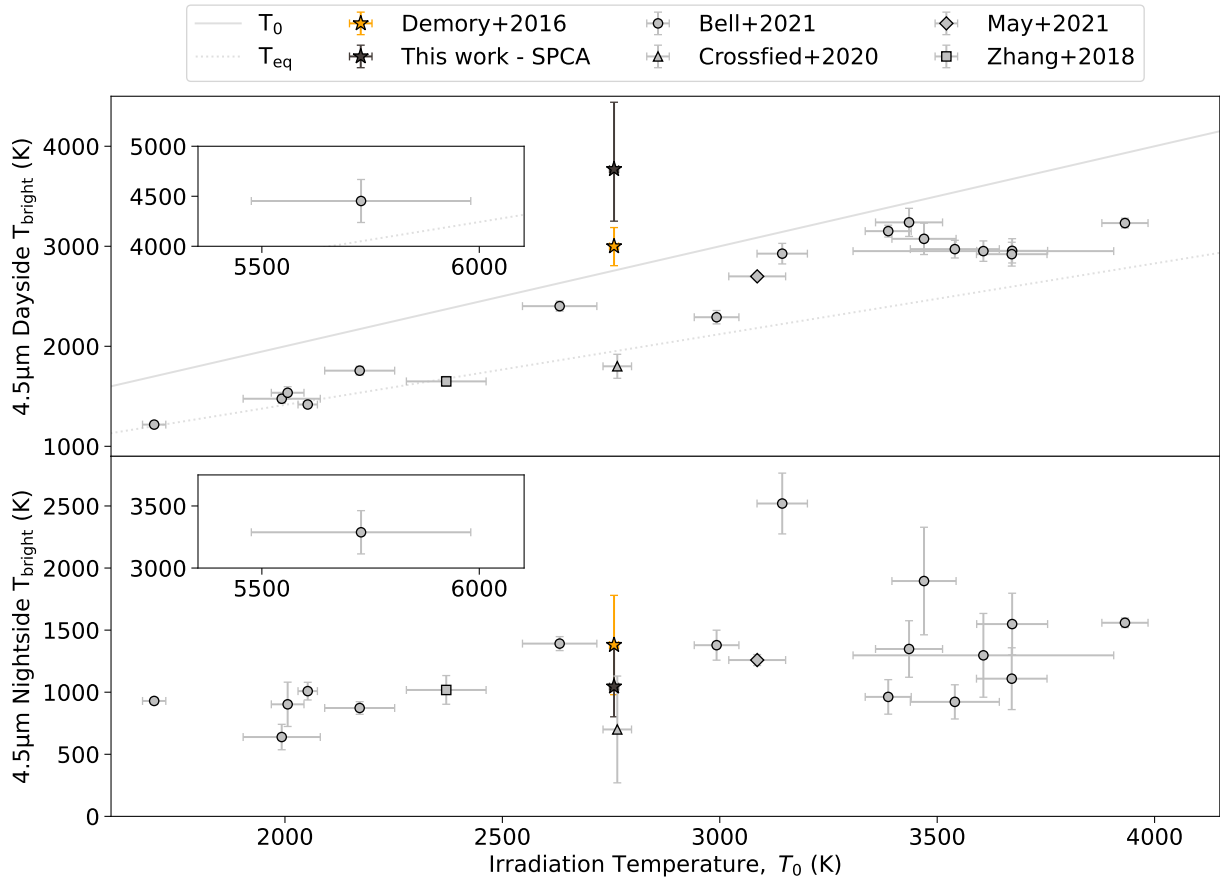


Figure 3. Dayside and nightside brightness temperatures plotted against irradiation temperature, for all circular exoplanets with published $4.5 \mu\text{m}$ phase curves. Values plotted as grey circles are from Bell et al. (2021), while grey triangles, squares and diamonds are from Crossfield et al. (2020), Zhang et al. (2018) and May et al. (2021), respectively. The gold and black values for 55 Cnc e are from D16b and this work, respectively. In the top plot, the dotted grey line represents the equilibrium temperature while the solid grey line represents the irradiation temperature. The extremely hot dayside brightness temperature for 55 Cnc e is qualitatively consistent with a temperature inversion and $4.5 \mu\text{m}$ emission due to SiO.

a dayside magma ocean evaporate into the atmosphere. Lava planets with silicate atmospheres are prone to temperature inversions due to UV absorption by SiO vapour (Ito et al. 2015; Zilinskas et al. 2022). In particular, for a stellar brightness temperature of 5172 K, the expected dayside brightness temperature at $4.5 \mu\text{m}$ is ~ 3100 K due to an SiO band, which is consistent with our results. Moreover, Nguyen et al. (2022) showed that the balance between UV heating and cooling of SiO leads to very hot stratospheric temperatures everywhere on the dayside, further enhancing the eclipse depth.

4. CONCLUSION

We have re-reduced and re-analyzed the 55 Cnc e photometric data collected by Spitzer in 2013 and published by Demory et al. (2016a). Even though our re-analysis largely followed D16b, our best-fit results, shown in Figure 2, differ from theirs. We have highlighted the potential origins of these discrepancies in Appendix A: pho-

tometric extraction strategy is the most likely culprit. We found a phase offset of 12_{-18}^{+21} degrees west, as opposed to D16b who reported a significant eastward offset, 2σ away from SPCA’s value. The negligible phase offset and low nightside flux are consistent with poor heat transport on an ultra-hot planet, while the large dayside flux could be a sign of a dayside inversion due to the SiO absorption of UV and re-emission at $4.5 \mu\text{m}$.

The James Webb Space Telescope (JWST) will soon observe several lava planets including K2-141b (Dang et al. 2021; Espinoza et al. 2021), GJ 367b (Zhang et al. 2021a) and 55 Cnc e (Hu et al. 2021; Brandeker et al. 2021), hopefully answering some questions regarding these exotic worlds.

5. ACKNOWLEDGEMENTS

S.M. acknowledges support from the Rubin Gruber Summer Undergraduate Research Award (SURA). This work would not have been possible without the help

of the members of the McGill Exoplanet Characterization Alliance (MEChA), the Institute for Research on Exoplanets (iREx), and the McGill Space Institute (MSI). L.D. acknowledges support in part through the Technologies for Exo-Planetary Science (TEPS) PhD Fellowship, and the Natural Sciences and Engineering Research Council of Canada (NSERC)’s Postgraduate Scholarships-Doctoral Fellowship. This work is based on archival data obtained with the Spitzer Space Tele-

scope, which is operated by the Jet Propulsion Laboratory, California Institute of Technology under a contract with NASA.

Facilities: Spitzer Space Telescope

Software: SPCA, `batman`⁴ (Kreidberg 2015), `emcee`⁵ (Foreman-Mackey et al. 2013), `corner`⁶ (Foreman-Mackey 2016), Spitzer Heritage Archive (IRSA 2022), `astropy`⁷ (Astropy Collaboration et al. 2013, 2018), `numpy`⁸ (Harris et al. 2020)

APPENDIX

A. POTENTIAL CAUSES FOR DIFFERENT RESULTS

There are many possible sources for the discrepancies between our best-fit values and those of D16b. As can be seen in Table 1, we used the most up to date planetary parameters from Bourrier et al. (2018) for our fixed astrophysical parameters. As a test, we also performed an analysis using the same fixed planetary parameters as D16b and found very similar results to the ones shown in Figure 2 and Table 1, so the fixed planetary parameters are not the dominant source of discrepancy.

A.1. Data Reduction

After the reduction of the Spitzer/IRAC data, D16b grouped the frames in 30 s bins, or by a factor of 1500. As mentioned in Section 2.2, we bin the frames by datacube, or by a factor of 64, because it averages over any residual systematic flux modulations present in the datacube (Deming et al. 2011). For computing efficiency we further binned the data by an order of magnitude, bringing our final binning to a factor of 640, or 12.8 s bins. Further details concerning the binning in SPCA, and its effects or lack thereof on detector detrending, can be found in Dang et al. (2018) and Bell et al. (2021). We ran fits on data that was less binned than D16b, but only by a factor of 2-3 and found similar results as our fiducial analysis. We conclude that binning is unlikely to be the source of discrepancy.

A.2. Centroiding

IRAC detrending depends heavily on centroiding. As a result, choosing different centroiding methods will affect the decorrelation process and impacts the best-fit results. After experimenting with various centroiding methods, including 2D Gaussians, we elected to use a flux-weighted mean as it gave us the lowest photometric scatter. In contrast, D16b used two-dimensional Gaussian fitting, and do not mention testing alternative centroiding schemes. It is possible that our different centroiding strategies led to different astrophysical parameters.

A.3. Photometry

As explained in Section 2.3, we used a moving, soft-edge aperture of radius 2.2 pixels for our photometric scheme. In comparison, D16b used a fixed aperture with variable radius ranging from 2.6 to 3.4 pixels for each AOR. The aperture radius values for each AOR can be found in the Extended Table 1 of their article. D16b must have accounted for their variable aperture radius by adding an offset parameter for each AOR. It seems likely to us that these additional parameters could explain why we cannot reproduce the D16b results.

A.4. Astrophysical Model

D16b use a Lambertian function for the phase modulations of the planet, while SPCA uses a first-order sinusoidal phase variation model. The Lambertian function is an adequate approximation for reflected light, but the Spitzer/IRAC observations correspond to thermal emission. Nonetheless, D16b also experimented with a first-order sinusoidal model

⁴ <http://lkreidberg.github.io/batman/docs/html/index.html>

⁵ <https://emcee.readthedocs.io/en/stable/>

⁶ <https://corner.readthedocs.io/en/latest/>

⁷ <https://www.astropy.org>

⁸ <https://numpy.org>

and found best-fit results in agreement with their fiducial analysis. All other aspects of the astrophysical model were the same for both analyses.

B. UNCONSTRAINED ANALYSIS

As optical monitoring with MOST and CHEOPS exhibit phase modulation with amplitude greater than the secondary eclipse depth, we experiment with an unconstrained analysis by allowing the photometric phase variation to drop below the bottom of the eclipse. As explained in section 3.2, the large phase amplitude of our unconstrained analysis, listed in Table 2 is unlikely to be of the same nature as the phase variation observed in optical observations.

Table 2. Fixed, Free and Derived Parameters for the unconstrained analysis of 55 Cancri e

Parameters	SPCA Values - unconstrained	D16b Values
Fixed Astrophysical Parameters		
i (degrees)	$83.59^{+0.5}_{-0.4}$	$83.3^{+0.9}_{-0.8}$
P (days)	$0.7365474^{+0.0000013}_{-0.0000014}$	0.736539 ± 0.000007
T_0 (days)	$2457063.2096^{+0.0006}_{-0.0004}$	2455733.013 ± 0.007
a/R_*	3.52 ± 0.01	3.514 ± 0.62
e	0.05 ± 0.03	$0.061^{+0.065}_{-0.043}$
ω (degrees)	86^{+31}_{-33}	202^{+88}_{-70}
q_1	0.028609764174322733	0.028609764174322733
q_2	0.05544212401093798	0.05544212401093798
Stellar Effective Temperature (K)	5172 ± 18	5250^{+123}_{-172}
Stellar Surface Gravity ($\log_{10}(cm/s^2)$)	4.43 ± 0.02	$4.43^{+0.052}_{-0.14}$
Stellar Metallicity (dex)	0.35 ± 0.10 [Fe/H]	0.35 ± 0.10 [M/H]
checkPhase	False	True
Free Astrophysical Parameters		
R_P/R_*	$0.01623^{+0.00083}_{-0.00084}$	0.0187 ± 0.0007
F_P/F_*	$0.000176^{+0.000025}_{-0.000025}$	0.000154 ± 0.000023
Photometric precision (ppm)	$443.1^{+3.7}_{-3.6}$	363
A	$0.868^{+0.19}_{-0.15}$	Unknown
B	$0.212^{+0.14}_{-0.13}$	Unknown
Detector Hyper Parameters		
x knot resolution	84	Unknown
y knot resolution	64	Unknown
Derived Parameters		
Phase Semi-Amplitude (ppm)	172.2^{+34}_{-28}	75.8 ± 17
Phase Offset (degrees east)	-15.68^{+8}_{-7}	41 ± 12
Average Dayside Temperature (K)	3439^{+456}_{-397}	2999^{+188}_{-193}
Average Nightside Temperature (K)	-1185^{+427}_{-485}	1380 ± 400

C. INFLATING UNCERTAINTIES

We find that there is significant red noise in our residuals and as a result, we choose to inflate our uncertainties following Pont et al. (2006). The photometric RMS shown in Figure 4 is about twice as important as the expected Gaussian noise at the vertical dash-dotted line, as such we inflate our error bars by a factor of 2. We inflate the error bars by a factor of 2 for the free astrophysical parameters. For derived parameters, we double the standard deviation of the probability distributions used in the derivation.

D. TENTATIVELY RULING OUT HYDROGEN-DOMINATED ATMOSPHERE

Our planet-to-stellar radius ratio $(R_p/R_*)_{\text{spit}} = 0.01708 \pm 0.00168$ is in excellent agreement with the CHEOPS and TESS measurement of $(R_p/R_*)_{\text{cheops}} = 0.01693 \pm 0.00035$, and $(R_p/R_*)_{\text{tess}} = 0.01708 \pm 0.00024$, respectively

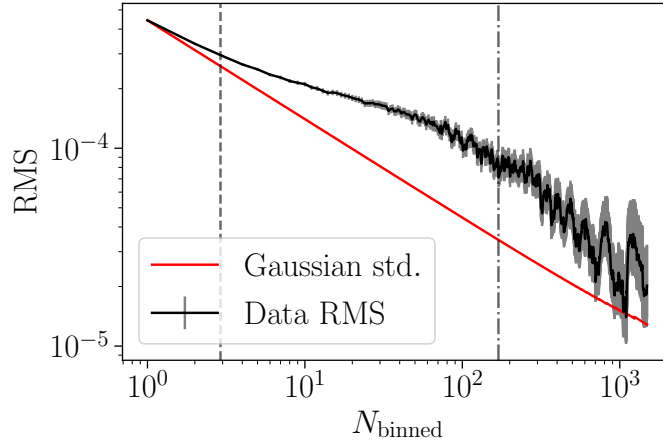


Figure 4. Binned residuals RMS plotted against bin size. The expected decrease in white noise is shown as a solid red line. The solid black line indicates the photometric residual RMS computed for different bin sizes N_{binned} . The lighter shaded area around the photometric residual RMS is the uncertainty that the MC3 package computed (Cubillos et al. 2017). The vertical grey dashed and dashdotted lines represent the number of bins contained in the duration of an occultation ingress/egress and in the duration of the entire transit/eclipse.

(Morris et al. 2021; Meier Valdés et al. 2022). This suggests that 55 Cnc e either has a high mean molecular mass atmosphere, a cloudy atmosphere, or no atmosphere at all. The atmospheric transit spectral feature can be approximated $2R_p N_H H / R_*^2$, where N_H is the number of atmospheric scale heights probed, and $H = k_B T / \mu g$ is the atmospheric scale height of the planet where T is the atmospheric temperature, μ is the atmospheric mean molecular mass, and g is the surface gravity (Cowan et al. 2015). Adopting the parametrization of Cowan & Agol (2011), $T = T_* (R_* / a)^{1/2} (1 - A_B)^{1/4} (2/3 - 5\epsilon/12)^{1/4}$ and assuming a Bond albedo of $A_B = 0.3$ and heat recirculation efficiency of $\epsilon = 0.2$, we estimate the atmospheric temperature of the planet as $T = 2290\text{K}$. Assuming we probe 4 scale heights, for a hydrogen-dominated atmosphere we estimate the amplitude of the transit spectral feature to be 1.61×10^{-4} . As the spectral feature is ~ 2.8 the quadrature sum of the uncertainties, this tentatively rules out a cloud-free hydrogen atmosphere at 2.8σ .

Table 3. Measured Transit Depths of 55 Cnc e

Parameters	Instrument	R_p/R_*	Transit Depth $(R_p/R_*)^2$
Demory et al. (2016b)	4.5 μm Spitzer	0.0187 ± 0.0007	0.000350 ± 0.000026
This work	4.5 μm Spitzer	0.01708 ± 0.00168	0.000292 ± 0.000057
Morris et al. (2021)	CHEOPS	0.01693 ± 0.00035	0.000287 ± 0.000012
Meier Valdés et al. (2022)	TESS	0.01708 ± 0.00024	0.000292 ± 0.000008

REFERENCES

- Angelo, I., & Hu, R. 2017, *AJ*, 154, 232, doi: [10.3847/1538-3881/aa9278](https://doi.org/10.3847/1538-3881/aa9278)
- Astropy Collaboration, Robitaille, T. P., Tollerud, E. J., et al. 2013, *A&A*, 558, A33, doi: [10.1051/0004-6361/201322068](https://doi.org/10.1051/0004-6361/201322068)
- Astropy Collaboration, Price-Whelan, A. M., Sipőcz, B. M., et al. 2018, *AJ*, 156, 123, doi: [10.3847/1538-3881/aabc4f](https://doi.org/10.3847/1538-3881/aabc4f)
- Bell, T. J., Dang, L., Cowan, N. B., et al. 2021, *MNRAS*, 504, 3316, doi: [10.1093/mnras/stab1027](https://doi.org/10.1093/mnras/stab1027)
- Bourrier, V., Dumusque, X., Dorn, C., et al. 2018, *A&A*, 619, A1, doi: [10.1051/0004-6361/201833154](https://doi.org/10.1051/0004-6361/201833154)

- Brandeker, A., Alibert, Y., Bourrier, V., et al. 2021, Is it raining lava in the evening on 55 Cancri e?, JWST Proposal. Cycle 1, ID. #2084
- Castan, T., & Menou, K. 2011, *The Astrophysical Journal Letters*, 743, L36
- Claret, A., & Bloemen, S. 2011, *A&A*, 529, A75, doi: [10.1051/0004-6361/201116451](https://doi.org/10.1051/0004-6361/201116451)
- Cowan, N. B., & Agol, E. 2011, *ApJ*, 729, 54, doi: [10.1088/0004-637X/729/1/54](https://doi.org/10.1088/0004-637X/729/1/54)
- Cowan, N. B., Greene, T., Angerhausen, D., et al. 2015, *PASP*, 127, 311, doi: [10.1086/680855](https://doi.org/10.1086/680855)
- Crossfield, I. J. M., Dragomir, D., Cowan, N. B., et al. 2020, *ApJL*, 903, L7, doi: [10.3847/2041-8213/abb71](https://doi.org/10.3847/2041-8213/abb71)
- Cubillos, P., Harrington, J., Lored, T. J., et al. 2017, *AJ*, 153, 3, doi: [10.3847/1538-3881/153/1/3](https://doi.org/10.3847/1538-3881/153/1/3)
- Dang, L., Cowan, N. B., Schwartz, J. C., et al. 2018, *Nature Astronomy*, 2, 220, doi: [10.1038/s41550-017-0351-6](https://doi.org/10.1038/s41550-017-0351-6)
- Dang, L., Cowan, N. B., Hammond, M., et al. 2021, A Hell of a Phase Curve: Mapping the Surface and Atmosphere of a Lava Planet K2-141b, JWST Proposal. Cycle 1, ID. #2347
- Dawson, R. I., & Fabrycky, D. C. 2010, *ApJ*, 722, 937, doi: [10.1088/0004-637X/722/1/937](https://doi.org/10.1088/0004-637X/722/1/937)
- Deibert, E. K., de Mooij, E. J. W., Jayawardhana, R., et al. 2021, *AJ*, 161, 209, doi: [10.3847/1538-3881/abe768](https://doi.org/10.3847/1538-3881/abe768)
- Deming, D., Knutson, H., Agol, E., et al. 2011, *ApJ*, 726, 95, doi: [10.1088/0004-637X/726/2/95](https://doi.org/10.1088/0004-637X/726/2/95)
- Demory, B.-O., Gillon, M., Madhusudhan, N., & Queloz, D. 2016a, *MNRAS*, 455, 2018, doi: [10.1093/mnras/stv2239](https://doi.org/10.1093/mnras/stv2239)
- Demory, B. O., Gillon, M., Deming, D., et al. 2011, *A&A*, 533, A114, doi: [10.1051/0004-6361/201117178](https://doi.org/10.1051/0004-6361/201117178)
- Demory, B.-O., Gillon, M., Seager, S., et al. 2012, The First Orbital Phase Curve of a Rocky Exoplanet, Spitzer Proposal
- Demory, B.-O., Gillon, M., de Wit, J., et al. 2016b, *Nature*, 532, 207, doi: [10.1038/nature17169](https://doi.org/10.1038/nature17169)
- Ehrenreich, D., Bourrier, V., Bonfils, X., et al. 2012, *A&A*, 547, A18, doi: [10.1051/0004-6361/201219981](https://doi.org/10.1051/0004-6361/201219981)
- Espinoza, N., Bello-Arufe, A., Buchhave, L. A., et al. 2021, The first near-infrared spectroscopic phase-curve of a super-Earth, JWST Proposal. Cycle 1, ID. #2159
- Esteves, L. J., de Mooij, E. J. W., Jayawardhana, R., Watson, C., & de Kok, R. 2017, *AJ*, 153, 268, doi: [10.3847/1538-3881/aa7133](https://doi.org/10.3847/1538-3881/aa7133)
- Fazio, G. G., Hora, J. L., Allen, L. E., et al. 2004, *ApJS*, 154, 10, doi: [10.1086/422843](https://doi.org/10.1086/422843)
- Fischer, D. A., Marcy, G. W., Butler, R. P., et al. 2008, *ApJ*, 675, 790, doi: [10.1086/525512](https://doi.org/10.1086/525512)
- Foreman-Mackey, D. 2016, *The Journal of Open Source Software*, 1, 24, doi: [10.21105/joss.00024](https://doi.org/10.21105/joss.00024)
- Foreman-Mackey, D., Hogg, D. W., Lang, D., & Goodman, J. 2013, *PASP*, 125, 306, doi: [10.1086/670067](https://doi.org/10.1086/670067)
- Hammond, M., & Pierrehumbert, R. T. 2017, *ApJ*, 849, 152, doi: [10.3847/1538-4357/aa9328](https://doi.org/10.3847/1538-4357/aa9328)
- Harris, C. R., Millman, K. J., van der Walt, S. J., et al. 2020, *Nature*, 585, 357, doi: [10.1038/s41586-020-2649-2](https://doi.org/10.1038/s41586-020-2649-2)
- Hu, R., Demory, B.-O., Seager, S., Lewis, N., & Showman, A. P. 2015, *ApJ*, 802, 51, doi: [10.1088/0004-637X/802/1/51](https://doi.org/10.1088/0004-637X/802/1/51)
- Hu, R., Brandeker, A., Damiano, M., et al. 2021, Determining the Atmospheric Composition of the Super-Earth 55 Cancri e, JWST Proposal. Cycle 1, ID. #1952
- Ingalls, J. G., Krick, J. E., Carey, S. J., et al. 2016, *AJ*, 152, 44, doi: [10.3847/0004-6256/152/2/44](https://doi.org/10.3847/0004-6256/152/2/44)
- IRSA. 2022, Spitzer Heritage Archive, IPAC, doi: [10.26131/IRSA543](https://doi.org/10.26131/IRSA543)
- Ito, Y., Ikoma, M., Kawahara, H., et al. 2015, *The Astrophysical Journal*, 801, 144
- Keating, D., & Cowan, N. B. 2017, *ApJL*, 849, L5, doi: [10.3847/2041-8213/aa8b6b](https://doi.org/10.3847/2041-8213/aa8b6b)
- Keles, E., Mallonn, M., Kitzmann, D., et al. 2022, *MNRAS*, doi: [10.1093/mnras/stac810](https://doi.org/10.1093/mnras/stac810)
- Kite, E. S., Fegley Jr, B., Schaefer, L., & Gaidos, E. 2016, *The Astrophysical Journal*, 828, 80
- Kreidberg, L. 2015, *PASP*, 127, 1161, doi: [10.1086/683602](https://doi.org/10.1086/683602)
- Kreidberg, L., Koll, D. D. B., Morley, C., et al. 2019, *Nature*, 573, 87, doi: [10.1038/s41586-019-1497-4](https://doi.org/10.1038/s41586-019-1497-4)
- Léger, A., Grasset, O., Fegley, B., et al. 2011, *Icarus*, 213, 1
- May, E. M., Komacek, T. D., Stevenson, K. B., et al. 2021, *AJ*, 162, 158, doi: [10.3847/1538-3881/ac0e30](https://doi.org/10.3847/1538-3881/ac0e30)
- May, E. M., Stevenson, K. B., Bean, J. L., et al. 2022, *AJ*, 163, 256, doi: [10.3847/1538-3881/ac6261](https://doi.org/10.3847/1538-3881/ac6261)
- Meier Valdés, E. A., Morris, B. M., Wells, R. D., Schanche, N., & Demory, B. O. 2022, arXiv e-prints, arXiv:2205.08560. <https://arxiv.org/abs/2205.08560>
- Morris, B. M., Delrez, L., Brandeker, A., et al. 2021, *A&A*, 653, A173, doi: [10.1051/0004-6361/202140892](https://doi.org/10.1051/0004-6361/202140892)
- NASA Exoplanet Archive. 2019, Confirmed Planets Table, Accessed on 2022/08/01 at 13:51, IPAC, doi: [10.26133/NEA1](https://doi.org/10.26133/NEA1)
- Nguyen, T. G., Cowan, N. B., Pierrehumbert, R. T., Lupu, R. E., & Moores, J. E. 2022, *MNRAS*, doi: [10.1093/mnras/stac1331](https://doi.org/10.1093/mnras/stac1331)
- Pont, F., Zucker, S., & Queloz, D. 2006, *MNRAS*, 373, 231, doi: [10.1111/j.1365-2966.2006.11012.x](https://doi.org/10.1111/j.1365-2966.2006.11012.x)
- Ridden-Harper, A. R., Snellen, I. A. G., Keller, C. U., et al. 2016, *A&A*, 593, A129, doi: [10.1051/0004-6361/201628448](https://doi.org/10.1051/0004-6361/201628448)

- Schwartz, J. C., Kashner, Z., Jovmir, D., & Cowan, N. B. 2017, *ApJ*, 850, 154, doi: [10.3847/1538-4357/aa9567](https://doi.org/10.3847/1538-4357/aa9567)
- Stevenson, K. B., Harrington, J., Fortney, J. J., et al. 2012, *ApJ*, 754, 136, doi: [10.1088/0004-637X/754/2/136](https://doi.org/10.1088/0004-637X/754/2/136)
- Sulis, S., Dragomir, D., Lendl, M., et al. 2019, *A&A*, 631, A129, doi: [10.1051/0004-6361/201936066](https://doi.org/10.1051/0004-6361/201936066)
- Tabernero, H. M., Allende Prieto, C., Zapatero Osorio, M. R., et al. 2020, *MNRAS*, 498, 4222, doi: [10.1093/mnras/staa2583](https://doi.org/10.1093/mnras/staa2583)
- Tamburo, P., Mandell, A., Deming, D., & Garhart, E. 2018, *AJ*, 155, 221, doi: [10.3847/1538-3881/aabd84](https://doi.org/10.3847/1538-3881/aabd84)
- Tsiaras, A., Rocchetto, M., Waldmann, I. P., et al. 2016, *ApJ*, 820, 99, doi: [10.3847/0004-637X/820/2/99](https://doi.org/10.3847/0004-637X/820/2/99)
- Werner, M. W., Roellig, T. L., Low, F. J., et al. 2004, *ApJS*, 154, 1, doi: [10.1086/422992](https://doi.org/10.1086/422992)
- Winn, J. N., Sanchis-Ojeda, R., & Rappaport, S. 2018, *NewAR*, 83, 37, doi: [10.1016/j.newar.2019.03.006](https://doi.org/10.1016/j.newar.2019.03.006)
- Winn, J. N., Matthews, J. M., Dawson, R. I., et al. 2011, *ApJL*, 737, L18, doi: [10.1088/2041-8205/737/1/L18](https://doi.org/10.1088/2041-8205/737/1/L18)
- Zhang, M., Dai, F., Hu, R., Knutson, H. A., & Lam, K. 2021a, The First and Only Multi-wavelength Map of an Ultra-short-period sub-Earth, JWST Proposal. Cycle 1, ID. #2508
- Zhang, M., Knutson, H. A., Wang, L., et al. 2021b, *AJ*, 161, 181, doi: [10.3847/1538-3881/abe382](https://doi.org/10.3847/1538-3881/abe382)
- Zhang, M., Knutson, H. A., Kataria, T., et al. 2018, *AJ*, 155, 83, doi: [10.3847/1538-3881/aaa458](https://doi.org/10.3847/1538-3881/aaa458)
- Zieba, S., Zilinskas, M., Kreidberg, L., et al. 2022, arXiv e-prints, arXiv:2203.00370. <https://arxiv.org/abs/2203.00370>
- Zilinskas, M., van Buchem, C., Miguel, Y., et al. 2022, arXiv e-prints, arXiv:2202.04759. <https://arxiv.org/abs/2202.04759>